Applied Geometry Optimization of an Innovative 3D-Printed Wet-Scrubber Nozzle with a Lattice Boltzmann Method

Felix Reinke[1],*, Nicolas Hafen[1], Marc Haussmann[2], Michael Novosel[3], Mathias J. Krause[1,4], and Achim Dittler[1]

Dedicated to Prof. Dr. Thomas Hirth on the occasion of his 60th birthday

In contrast to conventional dry separators, new types of wet scrubbers with innovative nozzle geometries are capable of separating submicron particles with comparatively low pressure drop. As those geometries can easily be adapted using 3D-printing manufacturing, an applied geometry optimization can lead to a fast and cost-efficient product development cycle. In this study, the lattice Boltzmann method is used to optimize the pressure drop associated with a novel nozzle design. Simulated pressure drop data are validated with experimentally determined ones. By replacing originally installed ellipsoid-shaped bluff bodies with foil-shaped structures according to the 4-digit NACA-series, an optimization approach regarding the resulting pressure drop is described.

1 Introduction

When processing metals by grinding, brushing and polishing, fine metal particles are produced, which considerably consist of the PM_1 and $PM_{2.5}$ fraction. When mixed with air, those can lead to explosive atmospheres, posing serious risks at manufacturing sites. Due to progress in machining processes in recent years, the average size of resulting metal dust particles has continuously decreased. Their separation is, therefore, becoming significantly more complex eventually leading to the requirement of downstream filter elements. As a result, these filter elements are associated with an additional pressure drop and an increase in energy consumption. In contrast to conventional dry separators, new types of wet separators with innovative 3D-printed nozzle geometries are capable of separating the submicron particle fractions with a comparatively low pressure drop. Inside those nozzles a wet scrubbers' washing liquid is dispersed into a fine spray capturing the particles mid-air and separating them from the exhaust flow. Therefore, a fundamental understanding of the prevailing flow conditions is essential for the optimization of the 3D-printed nozzle geometry, which ensures the minimization of the pressure drop while maintaining a high separation efficiency. Using numerical flow simulations, the individual nozzle geometries can then be optimized efficiently in terms of flow guidance and pressure drop.

Numerical flow simulation can support the development in many steps of the product development cycle. Enabling pre-manufacturing studies for various designs, represents one major benefit of such an approach. Due to the degrees of freedom in terms of the geometry shapes by using rapid prototyping technology, the simulation is able to assist with the selection of design choices by predicting relevant physical properties. On the one hand it, therefore, expands the overall range of possible design studies and on the other hand reduces the amount of physical testing and premature

[1]Felix Reinke, Nicolas Hafen, Dr. Mathias J. Krause, Prof. Dr.-Ing. habil. Achim Dittler
felix.reinke@kit.edu
Karlsruhe Institute of Technology, Institute of Mechanical Process Engineering and Mechanics, Straße am Forum 8, 76131 Karlsruhe, Germany.

[2]Dr.-Ing. Marc Haussmann
cloudfluid GmbH, Emmy-Noether-Straße 17, 76137 Karlsruhe, Germany.

[3]Michael Novosel
ESTA Apparatebau GmbH & Co. KG, Gotenstraße 2–6, 89250 Senden, Germany.

[4]Dr. Mathias J. Krause
Karlsruhe Institute of Technology, Institute for Applied Numerical Mathematics, Englerstraße 2, 76131 Karlsruhe, Germany.

manufacturing steps, e.g., printing. This results in a reduction of time and cost in the whole development cycle. [1]

In this work, a single-phase numerical model to support the product development cycle for a 3D-printed wet-scrubber nozzle in the Reynolds number range from $Re = 53\,000$–$220\,000$ is proposed as a new development method. The applied open-source tool for numerical flow simulations is OpenLB [2, 3], which provides an implementation of the lattice Boltzmann method (LBM). Due to its highly efficient parallel algorithm, the LBM has a high potential in simulating turbulent flows with moderate computing time [4].

This research article is organized as follows. In Sect. 2, the fundamentals of the lattice Boltzmann method and subgrid-scale turbulence modeling are introduced. The numerical setup of the test case including its boundary conditions is described in Sect. 3. Evaluation methods for turbulence statistics, the validation approach using experimental data and the optimization approach are described additionally. The overall results are then reported in Sect. 4. Finally, conclusions and an outlook are provided in the final section.

2 Theoretical Background and Modeling

2.1 Lattice Boltzmann Method

For the numerical flow simulation, the lattice Boltzmann method (LBM) is used. The LBM is a discretization method for partial differential equations and is used to simplify the kinetic Boltzmann equation. A discrete set of particle populations $f_i(\mathbf{x}, t)$ represents the density of particles with the discrete set of velocities $\mathbf{c}_i = (c_{ix}, c_{iy}, c_{iz})$ at position $\mathbf{x}$ at time t. For three-dimensional applications, a set of 19 discrete velocities, for solving the slightly incompressible Navier-Stokes-Equation is used, commonly denominated as D3Q19. By discretizing the Boltzmann equation according to velocity as well as physical space and time the lattice Boltzmann equation (LBE) is given by

$$f_i(\mathbf{x} + \mathbf{c}_i, \ t + \Delta t) = f_i(\mathbf{x}, t) + \Omega_i(\mathbf{x}, t) \tag{1}$$

The LBE expresses that a particle population $f_i(\mathbf{x}, t)$ is moving with the velocity $\mathbf{c}_i$ to a neighboring position $\mathbf{x} + \mathbf{c}_i$ at the next time step $t + \Delta t$. At the same time the collision operator Ω_i is modeling the particle collisions through redistributing the particle population at every position [5]. A commonly used collision operator is the Bhatnagar-Gross-Krook (BGK) [5] operator (see Eq. (2)), which captures the relaxation of the population towards the thermodynamic equilibrium

$$\Omega_i(f) = -\frac{\Delta t}{\tau}\left(f_i(\mathbf{x}, t) - f_i^{eq}(\mathbf{x}, t)\right) \tag{2}$$

The therein contained relaxation time τ depends on the kinematic viscosity and specifies the speed of the equili-

brium adjustment process. The BGK-LBE is therefore given by

$$f_i(\mathbf{x} + \mathbf{c}_i\Delta t, \ t + \Delta t) = f_i(\mathbf{x}, t) - \frac{\Delta t}{\tau}\left(f_i(\mathbf{x}, t) - f_i^{eq}(\mathbf{x}, t)\right) \tag{3}$$

which can be divided into two sub steps occurring every discrete time step. First the collision step (right side of Eq. (3)), where the distributions are colliding, and second, the streaming step where the populations are propagated to the next position (left side of Eq. (3)).

2.2 Subgrid-Scale Turbulence Modeling in LBM

One of the characteristic properties of turbulence motion is its multiscale character, which means that turbulent eddies appear on different time and length scales [6]. For modeling the motion on these scales different approaches exist. However, in the following only the large-eddy simulation (LES) shall be in focus. For an in-depth overview of the different approaches and their implementation in the LBM, the interested reader is referred to Haussmann [7]. The main idea of LES is to resolve large eddies, but to model the effect of small eddies. To describe the interaction between the unresolved and resolved flow patterns, a subgrid-scale (SGS) model is necessary. A commonly used SGS is the Smagorinsky model [8]. The Smagorinsky model introduces an artificial dissipation to model the influence of the non-resolved scales. Malaspinas et al. [9] showed a detailed analysis of the Smagorinsky model and its consistent implementation in LBM.

3 Simulation Setup

3.1 Numerical Setup of the Wet-Scrubber Nozzle

In this work, a new innovative 3D-printed wet-scrubber nozzle was numerically and experimentally investigated. In order to reduce the complexity of the framework, all numerical calculations were done assuming single-phase flow. By limiting the numerical approach, the overall geometry can be simplified by omitting the elements of the nozzle used to insert and promote the washing fluid.

The computational domain is depicted in Fig. 1 and is divided into three different sections, the manifold, the nozzle and the outlet. The dimensions of the three regions in all spatial directions (x, y and z) are listed. The first section represents the manifold with an angular profile. The inlet plane is marked accordingly. The second section states the nozzle geometry. In a multiphase consideration, the washing-fluid would be dispersed and would move alongside the aerosol. The installed bluff bodies with ellipsoid shape serve the purpose of artificial flow resistors to accelerate and deceleration the fluid, which poses favorable condition for particle separation.
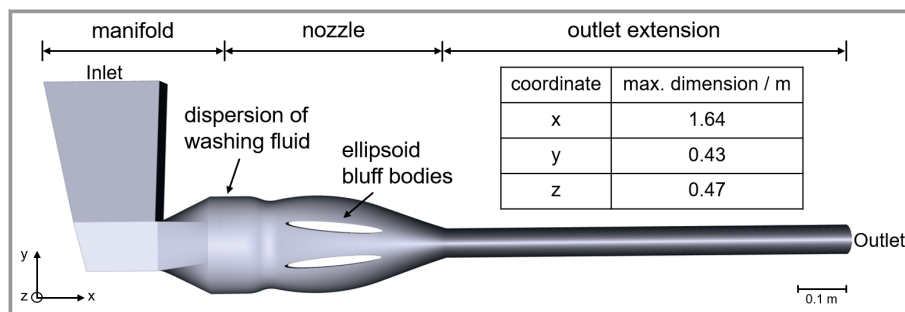
Figure 1. Representation of the computational domain in a multi-phase flow consideration.

The third section is an artificial outlet extension to minimize the effect of the boundary conditions on the flow field of interest. The outlet extension length is eight times the hydraulic diameter of the original outlet surface. The outlet plane is marked.

3.2 Initial and Boundary Conditions

In the following section, the inlet and boundary conditions used in this study are described and linked to literature for a detailed consideration.

For the inlet, the velocity boundary condition as proposed by Latt (BC4) [11] is used. The wall is described by the bounce-back approach [5]. The implemented ellipsoids are described by the approach of Bouzidi et al. [12] to reduce the aberrations of curved objects due to the staircase approximation of the bounce-back approach. The outflow condition uses a wet-node equilibrium boundary condition (see Haussmann et al. [4]).

A Smagorinsky-LES modeling with the BGK collision operator and a Smagorinsky constant of $C = 0.15$ is used to describe the fluid dynamics. The inflow velocity profile is a power law profile with an exponent of 1/7 perturbed by turbulence intensity of 5 %.

3.3 Turbulence Statistical Evaluation Method

The statistic method used for evaluating the LES in this research article is proposed by Ries et al. [13] who recommends minimum total record lengths for evaluation of engineering applications to accomplish desired accuracy. By using the statistic method, it is assumed that Taylor's hypothesis of "frozen turbulence" is fulfilled [14]. In the case of stationary turbulent flows, two integral time scales pass to get a statistically decorrelated signal. As statistic quantity, the root mean square of the velocity is chosen. By selecting the sampling error to $\varepsilon = 3.36\%$, the characteristic length (inlet diameter of the nozzle) to $l_c = 0.2$ m and the characteristic velocity to $U_c = 35$ m s^{-1}, the average sampling time calculates with

$$t_{av} = \frac{l_c}{U_c \varepsilon^2} \tag{4}$$

to $t_{av} = 5$ s. Note that for Reynolds number smaller than $Re = 215\,176$, the sampling error is larger for the same average sampling time. Since the relevant Reynolds number is $Re = 215\,176$, the statistics were selected for this case and kept constant.

3.4 Validation Method

In order to validate the simulation, the numerical pressure drop results are compared to experimental pressure drop data. The data was sampled using the hand-held measurement system Testo 512 with a measurement range from 0–200 hPa with an error of 0.5 % from the expected value. The first experimental pressure measuring point measures the pressure before the fluid is entering the nozzle. The second experimental measuring point measures the pressure outside of the nozzle. An experimental measuring point directly at the nozzle outlet is, due to space restrictions, not possible. However, the assumption is made that at the outlet plane of the nozzle the same pressure applies as in the chamber where the nozzle is installed. The same conditions apply for the reference sampling slices in the simulated test case as shown in Fig. 2. This figure also shows the pressure course along the middle of the nozzle. A homogenous pressure distribution along the nozzle can be seen. The pressure in the manifold is higher. The pressure decreases the closer it gets to the artificial outlet extension. The pressure course can be depicted realistically. To calculate the numerically obtained pressure value of one slice, a local mean of the pressure values of the slice is determined and time averaged. The pressure difference between both measuring planes was calculated and compared to experimental values for volume flows between 1000–4000 m^{3}h^{-1}, where 4000 m^{3}h^{-1} represents a typical operating point for wet scrubbers. By using the diameter of the nozzle of $l_c = 0.2$ m as characteristic length, those volume flows result in Reynolds values from $Re = 53\,795$–$215\,179$.

In order to be able to represent the influences of discretization errors and deviations on the numerical pressure drop result, an error norm must be defined. In this research article, the L_2-error standard is used as follows

$$L_2 = \left(\frac{\sum_x \left(q_n(x,t) - q_{ref}(x,t) \right)^2}{\sum_x q_{ref}^2(x,t)} \right)^{0.5} \tag{5}$$
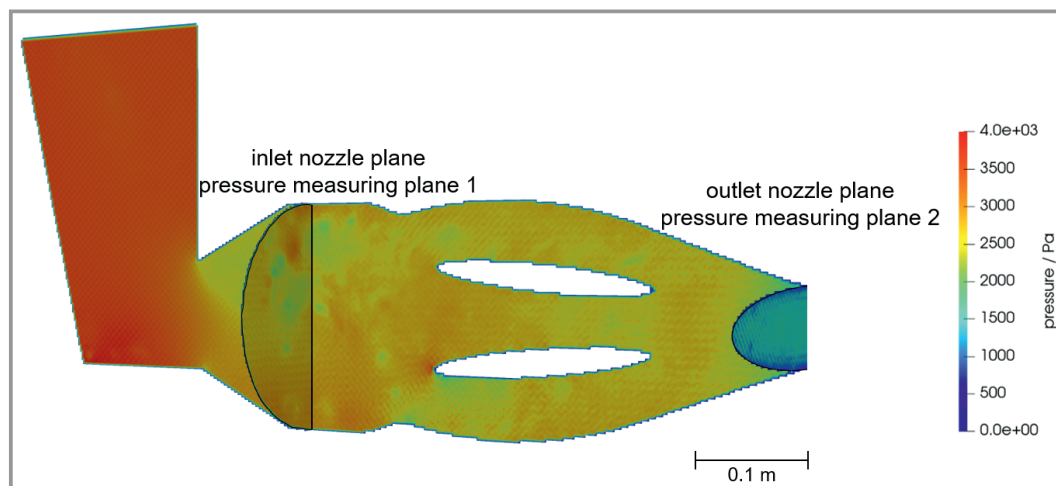
Figure 2. Pressure field at the middle of the computational domain. The selected planes for calculating the pressure drop along the nozzle are shown as well.

$q_{ref}(x,t)$ stands here for the reference solution and $q_n(x,t)$ for the numeric solution. As analytical solution pressure drop data at the resolution of $N = 100$ are selected. The resolution N calculates as a fraction of the characteristic length $l_c = 0.2$ m to the lattice width Δx. For numerical solution pressure drop data at resolutions of $N = 80$ and $N = 40$ are chosen.

3.5 Bluff Body Shape Optimization Approach

In order to optimize the pressure drop of the new wet-scrubber nozzle, an analyzation of the shape of the bluff bodies is necessary. It is worth noting that due to manufacturing restrictions the outer shape of the nozzle and the upstream inflow manifold are immutable.

As stated in [15], drag optimized shapes such as NACA-airfoils are capable of having lower flow resistance compared to ellipsoid shaped bluff bodies. Due to the extreme high variety of different NACA-airfoils, the selection of eligible profiles is reduced to the 4-digit symmetric series from [16]. The comparability to ellipsoid shaped bluff bodies is given due to the symmetrical shape. Another important factor for the selection of NACA-airfoils in the present study is the big reference data basis (e.g., [16]). Worth mentioning at this point is that no dedicated wall model is applied (neither for the ellipsoid shaped bluff bodies nor the NACA airfoils) to represent the boundary layer. This is due to the fact that the implementation of wall functions in LBM is not straight forward reflected by the huge number of existing boundary scheme approaches [4]. Also, there is to the best knowledge of the author, currently no implementation for boundary layers with pressure gradients and detachment implemented in LBM. Another reason for neglecting the wall function is the increase in complexity due to the wall-near treatment [17]. Letting the wall function aside also results in an enormous decrease in the computational cost [18]. The reason for the latter is the good accordance of simulated values against experimental data as shown in Sect. 4.

The optimization approach is not only considering the pressure drop of the nozzle (since this optimization would lead to an elimination of the ellipsoid shaped bluff bodies) but also the turbulence energy at the outlet plane. Considering high turbulence intensities as good for inertial deposition of particles on droplets, high values are desired. To conclude, we want to achieve relative high turbulence intensity along the nozzle and at the outlet with a low total pressure drop.

The first optimization approach is to implement a NACA profile with the same reference area as the ellipsoid bluff bodies with the same angle of attack (AOA) and the same length. The reference area is here defined as the area of the lateral cutting plane. This results in a NACA profile with a thickness to length ratio of 27.46 %. This profile is named 0027 in the following. Subsequently, the NACA profiles (0012, 0015, 0018, 0021, 0025) were investigated under the same conditions. The simulated profiles and their thickness to length ratio χ are shown in Fig. 3.

All simulations of the optimization approach were made at a Reynolds number $Re = 215\,179$ at lattice width of $\Delta x = 0.0025$, which results in a resolution $N = 80$ and in a total of approximately $4 \cdot 10^6$ calculation cells.

4 Results

In this section the results of the simulated pressure drop of a wet-scrubber nozzle are analyzed. At first, the flow through the nozzle is described. Then, the ability to reproduce the pressure drop of the already existing 3D-printed nozzle is described. Subsequently, an optimization approach regarding the shape of the ellipsoid bluff bodies is made.
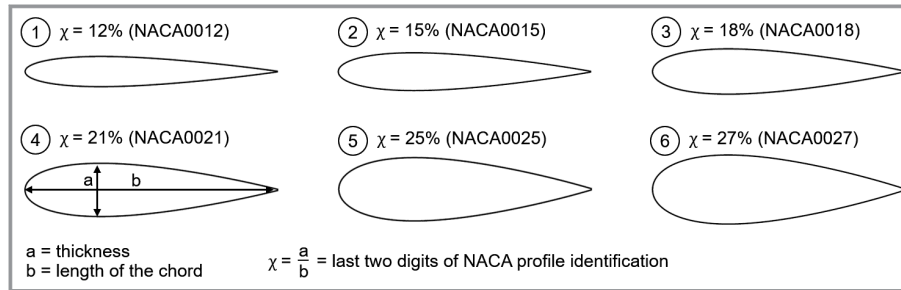
Figure 3. Representation of six selected symmetrical NACA profiles (00xx series) with different thickness a, length of the chord b and its ratio χ for the bluff body shape optimization.

4.1 Characterization of the Flow through the Nozzle

Fig. 4 depicts a clip representation of the instantaneous velocity profile along the middle of the nozzle for a Reynolds number of $Re = 215\,179$ at a resolution of $N = 80$. Note that the artificial outlet extension is truncated in the visualization. It can be seen that along the transition area from the manifold to the nozzle, the angular tapering has a big impact on the flow guidance upon the entry of the nozzle. Following the lower part of the entrance of the nozzle high flow velocities can be seen. These high flow velocities in the lower part of the nozzle occurring from the inlet to the outlet and resulting due to the non-uniform inlet flow. Above the high flow velocities at the inlet of the nozzle an area of swirled streamlines, and therefore high turbulence intensity, can be seen. The flow passing the lower ellipsoid exposes significantly higher flow velocities compared to the upper part. Here, medium flow velocities can be observed. Above the upper ellipsoid, high flow velocities can be seen at the start of the flow around the ellipsoid due to the flow redirection of the flow obstacle.
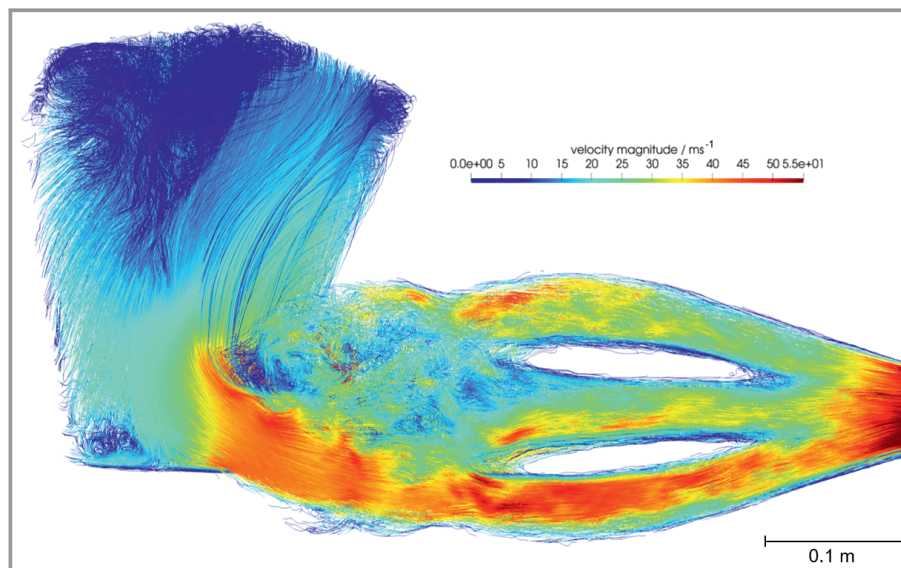
The turbulence intensity along the middle of the nozzle is presented in Fig. 5 (left). Additionally, the intensity at the inlet slice (see inlet plane in Fig. 2) is presented as well (right). The magnitude of the intensity is colored with the same scale in both depictions. It can be seen that in regions apart from the main flow (low turbulence intensities) the intensity reaches its maximum due to different flow velocities. Due to the bluff bodies, the turbulence intensity decreases to a moderate level. This is due to the rectifying property of the bluff bodies. In the trailing area of the ellipsoids, high intensities can be seen. At the outlet, where high flow velocities appear, the intensity is comparably low.

4.2 Validation Results

Fig. 6 shows the numerically and experimentally determined pressure drop for different Reynolds numbers. Square symbols represent the experimental values. Circle and triangle symbols represent the simulated values for resolutions between $N = 40$–100. By increasing the resolution from $N = 40$ to $N = 80$, the simulated values can be observed to approximate the experimental results. At a resolution of $N = 100$, the simulated pressure drop yields an excellent accordance with the experimental pressure drop data. For a profound glimpse in the deviations, Fig. 7 represents the L_2-error of the simulation. As Fig. 7 shows, the L_2-errors decrease by doubling the resolution from $N = 40$ to $N = 80$ for different Reynolds numbers. The resolution of $N = 100$ is not shown in Fig. 7 since it represents the reference solution for the L_2-error calculation. The error of convergence (EOC) of the simulations for different Reynolds numbers lies in the range between $2.68 \leq \text{EOC} \leq 2.99$ due to a large initial error. For the application case grid independence is shown. The resolution $N = 80$ is selected for

Figure 4. Clip representation of the nozzle with manifold. The clip halved the nozzle. The instantaneous velocity at $t = 15\,s$ is represented by streamlines and its magnitude is colored.
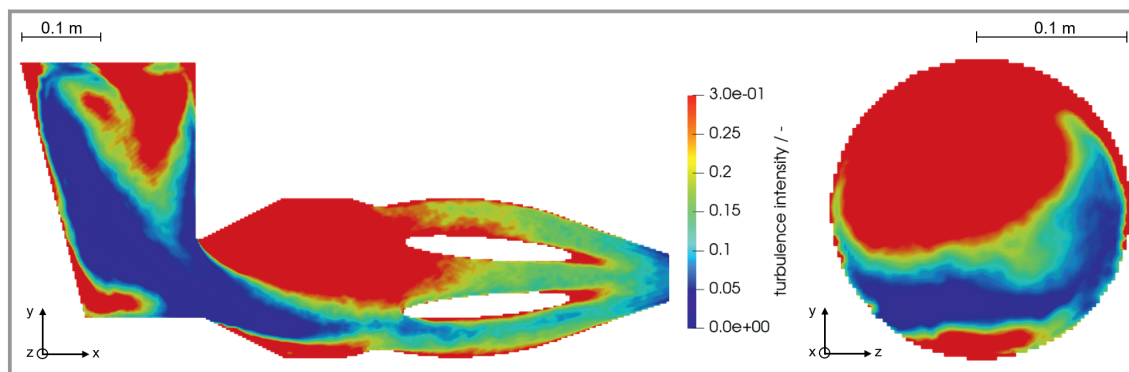
Figure 5. Turbulence intensity along the middle slice of the nozzle (left) and turbulence intensity along the inlet slice of the nozzle (right) at a resolution of $N = 80$ at time $t = 15$ s and Reynolds number $Re = 215\,179$.

further studies due to feasible simulation time and good accordance to the experimental dataset.

4.3 Bluff Body Shape Optimization Approach

In order to optimize the pressure drop in the nozzle, a design study of the bluff bodies is made. Fig. 8 shows the pressure drop over the turbulence intensity for different NACA profiles at Reynolds number $Re = 215\,179$. As reference, the value for the ellipsoid bluff bodies is represented as square. From this reference point, the optimization approach is made. In general, it can be seen that NACA profiles with a larger thickness to chord ratio result in a higher pressure drop and a higher turbulence intensity at the outlet plane. It is worth noting that due to resolution limitations of the fine tail of the NACA profiles, the profiles with a smaller thickness to chord length ratio than 12 % are not well represent-

ed in the simulation. As expected, the 0027 profile has a higher pressure drop and higher turbulence intensity compared to the ellipsoid bluff body. This is due to its total blockage of the nozzle and the therefore stronger tapering of the flow channel in the nozzle. By choosing the profile with the lowest pressure drop, 0012 profile, the pressure drop can be reduced by about 60 Pa.

5 Discussion and Conclusion

The purpose of this study is to develop a numerical model for an applied geometry optimization of an innovative 3D-printed wet-scrubber nozzle with regard to the pressure drop in a Reynolds number range from $Re = 53\,000$–$220\,000$ to reduce the development time of the product development cycle.

Thereby, a Smagorinsky-LES turbulence model is applied with LBM. The simulated pressure drop is statistically evaluated and compared with experimental values. For a resolution of $N = 80$ the L_2-error related to a resolution of $N = 100$ is $L_2 \leq 0.0754$ for the whole Reynolds number range. Taking the measurement uncertainty of 5 % from the expected value into account, it can be stated that the model is able to retrieve the pressure drop exactly, when a sufficiently high resolution is selected. A resolution of $N = 80$ is proposed due to reasonable computing time with sufficient accuracy. As mentioned in Sect. 3, no dedicated wall function is applied so it is remarkable to recover the pressure drop at such a wide Reynolds number span with the accuracy exhibited.

Subsequently, the bluff body shape optimization approach regarding the artificial ellipsoid bluff body is made to reduce the pressure drop at constant turbulence intensity at the outlet of the nozzle. In this study, the symmetric 4-digit NACA series is chosen. Due to resolution limitations regarding the fine tail of the NACA profiles, only profiles with a higher thickness to
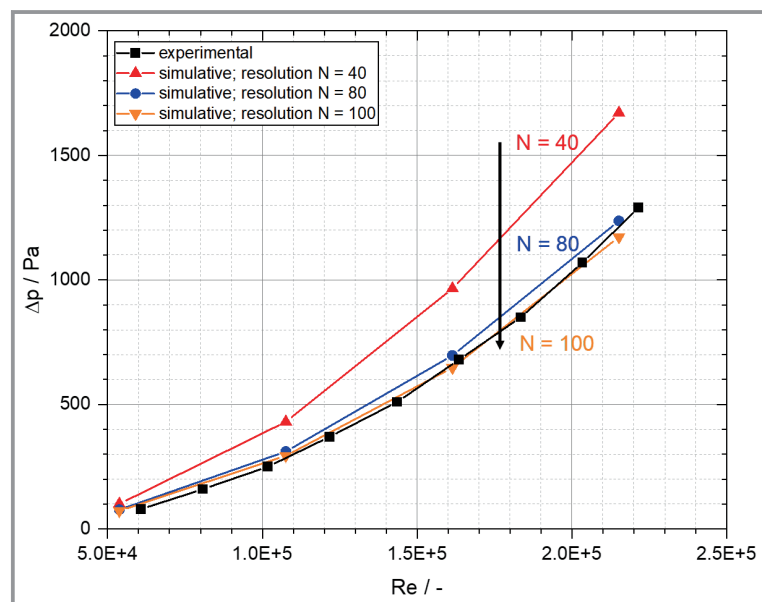

Figure 6. Pressure drop of the wet-scrubber nozzle versus the Reynolds number for resolutions of $N = 40$, $N = 80$ and $N = 100$ and as well as experimental data.
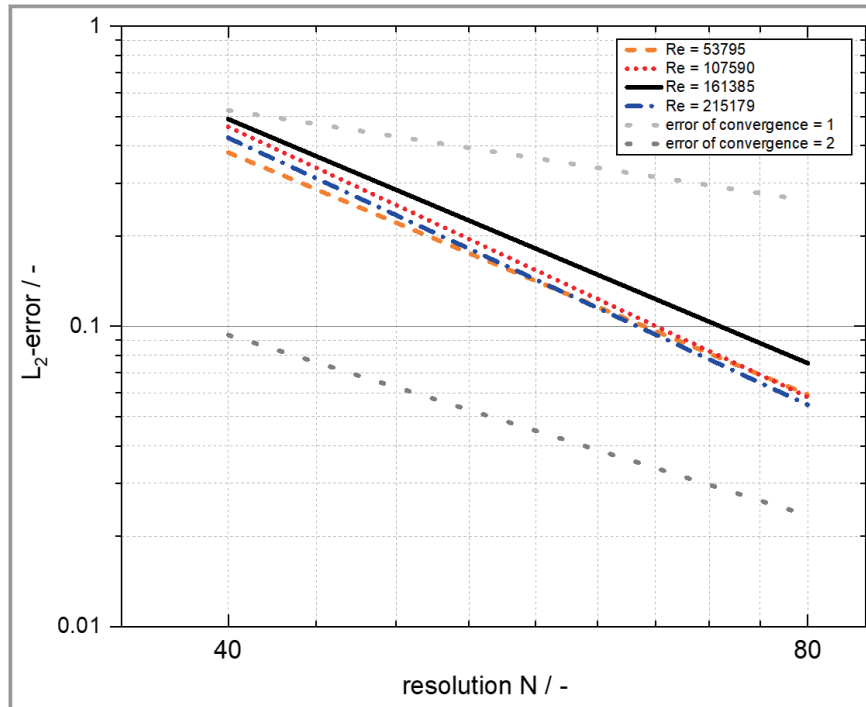
Figure 7. L_2-error norm of the pressure drop for Reynolds numbers Re = 53 795–215 179 for the resolution N = 40 and N = 80 with respect to N = 100. The error of convergence for first and second order are shown as reference.
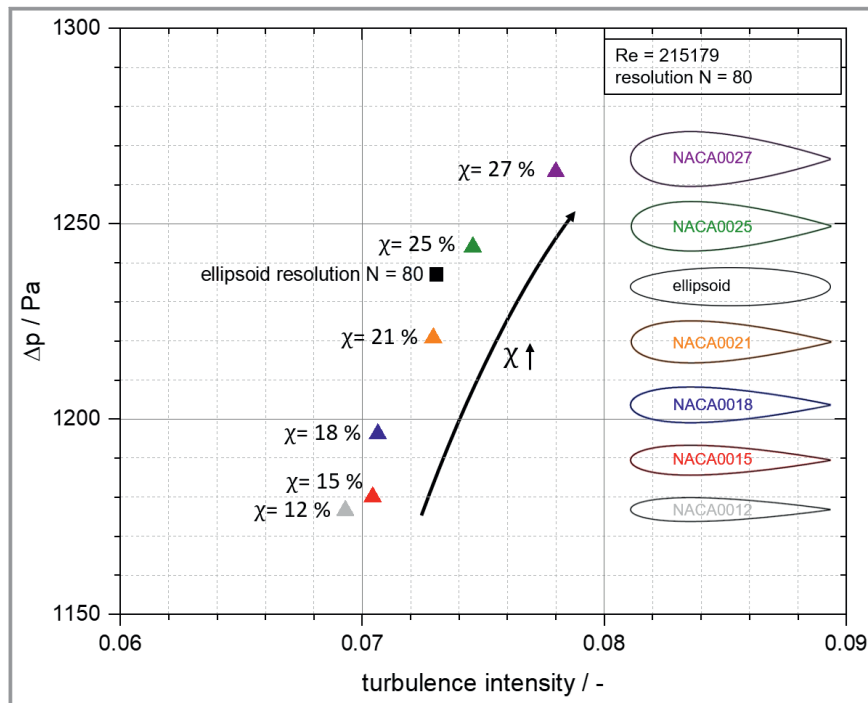

Figure 8. Pressure drop versus turbulence intensity at the outlet plane for six NACA profiles and an ellipsoid bluff body at resolution N = 80. The Reynolds number and the angle of attack (AOA) is kept constant.

chord length ratio of 12 % are considered for further optimizations. By comparing the 0027 profile, which has the same area perpendicular to the main flow direction, to the original ellipsoid shaped bluff bodies, the NACA profile has a higher pressure drop. This is due to the high ratio of thickness to length of the chord, which results in a larger total blocking area at the inflow side of the bluff bodies. The NACA profile 0012 is proposed as optimum shape due to the maximum reduction of the pressure in this study by Δp = 60 Pa, which leads to a decrease of air performance of 67 W.

A short comparison of expenditure of time between experimental and simulation is made to assess the benefit of the model for the product development cycle. The simulations were performed on 5 nodes with 40 cores each with Intel Xeon Gold 6230. Each simulation took about 50 h. The nozzle is printed by a Stratasys Dimension SST1200es printer with ABS as material. The printing method is fuse deposition modeling. Printing the nozzle in three parts and assembling them takes about 72 h in total, excluding the following experimental procedure. In summary, the development time of a single nozzle can be reduced by 30 % for each investigated variation in this setup.

It can be concluded that the developed and validated LBM-LES toolbox is able to model the pressure drop in a 3D-printed wet-scrubber nozzle considering single-phase flow in a Reynolds number range from Re = 53 000–220 000. Therefore, the model can now be used to optimize the flow guidance and therefore the pressure drop and separation efficiency of the nozzle. The first optimization study is made by changing the bluff body from ellipsoid shape to airfoil shape. A reduction of the pressure drop is seen.

Nevertheless, further investigations to assess the influence of a dedicated wall function on the accuracy should be made. Additionally, the single-phase flow simulation and the result-

ing pressure drop is only one part of the application-related pressure drop. As mentioned in [19], an additional pressure drop contribution due to the dispersion and acceleration of the water in a real multiphase flow application of the nozzle could be considered (see Fig. 1). Nonetheless, the single-phase flow model presented in this study can already be of great value for the optimization of the nozzle bluff body shapes and the related separation efficiency and energy consumption.

Symbols used

a	[m]	thickness
b	[m]	length of the chord
c	[m s^{-1}]	velocity
C	[–]	Smagorinsky constant
f	[–]	particle populations
N	[–]	resolution
p	[Pa]	pressure
Re	[–]	Reynolds number
t	[s]	time
x	[–]	position

Greek symbols

ε	[%]	sampling error
τ	[–]	relaxation time
Ω	[–]	collision operator
χ	[–]	fraction of the thickness to length of the chord of a NACA profile

Sub- and Superscripts

i	related to the i-th population of f

Abbreviations

ABS	acrylonitrile butadiene styrene
AOA	angle of attack
BGK	Bhatnagar-Gross-Krook
LBM	lattice Boltzmann method
LES	large-eddy simulation
NACA	National Advisory Committee for Aeronautics (here, serial prefix)
SGS	subgrid-scale model

References

[1] C. Lange, P. Barthelmäs, T. Rosnitschek, S. Tremmel, F. Rieg, *Appl. Sci.* **2021**, *11 (14)*, 6552. DOI: https://doi.org/10.3390/app11146552

[2] M. J. Krause, S. Avis, D. Dapelo, N. Hafen, M. Haußmann, M. Gaedtke, F. Klemens, A. Kummerländer, M.-L. Maier, A. Mink, J. Ross-Jones, S. Simonis, R. Trunk, *OpenLB Release 1.3: Open Source Lattice Boltzmann Code*, Zenodo **2019**.

[3] M. J. Krause, A. Kummerländer, S. J. Avis, H. Kusumaatmaja, D. Dapelo, F. Klemens, M. Gaedtke, N. Hafen, A. Mink, R. Trunk, J. E. Marquardt, M.-L. Maier, M. Haussmann, S. Simonis, *Comput. Math. Appl.* **2021**, *81*, 258–288. DOI: https://doi.org/10.1016/j.camwa.2020.04.033

[4] M. Haussmann, F. Ries, J. B. Jeppener-Haltenhoff, Y. Li, M. Schmidt, C. Welch, L. Illmann, B. Böhm, H. Nirschl, M. J. Krause, A. Sadiki, *Computation* **2020**, *8 (2)*, 43. DOI: https://doi.org/10.3390/computation8020043

[5] T. Krüger, H. Kusumaatmaja, A. Kuzmin, O. Shardt, G. Silva, E. M. Viggen, *The Lattice Boltzmann Method*, Springer International Publishing, Cham **2017**.

[6] J. H. Ferziger, M. Peric, *Numerische Strömungsmechanik*, Springer, Berlin **2008**.

[7] M. Haussmann, *Lattice Boltzmann Methods for Turbulent Flows – Application to Coriolis Mass Flowmeter*, Dissertation, Karlsruhe **2020**. DOI: https://doi.org/10.5445/IR/1000124435

[8] J. Smagorinsky, *Mon. Weather Rev.* **1963**, *91 (3)*, 99–164. DOI: https://doi.org/10.1175/1520-0493(1963)091<0099:GCEWTP>2.3.CO;2

[9] O. Malaspinas, P. Sagaut, *J. Fluid Mech.* **2012**, *700*, 514–542. DOI: https://doi.org/10.1017/jfm.2012.155

[10] W. Barth, *Staub* **1959**, *19*, 175–180.

[11] J. Latt, B. Chopard, O. Malaspinas, M. Deville, A. Michler, *Phys. Rev. E: Stat., Nonlinear, Soft Matter Phys.* **2008**, *77 (5 Pt 2)*, 56703. DOI: https://doi.org/10.1103/PhysRevE.77.056703

[12] M. Bouzidi, M. Firdaouss, P. Lallemand, *Phys. Fluids* **2001**, *13 (11)*, 3452–3459. DOI: https://doi.org/10.1063/1.1399290

[13] F. Ries, K. Nishad, L. Dressler, J. Janicka, A. Sadiki, *Theor. Comput. Fluid Dyn.* **2018**, *32 (6)*, 733–752. DOI: https://doi.org/10.1007/s00162-018-0474-0

[14] G. I. Taylor, *Proc. R. Soc. London, Ser. A* **1938**, *164 (919)*, 476–490. DOI: https://doi.org/10.1098/rspa.1938.0032

[15] B. R. Munson, *Fundamentals of fluid mechanics*, 6th ed., Wiley, Hoboken NJ **2009**.

[16] E. N. Jacobs, K. E. Ward, R. M. Pinkerton, *The characteristics of 78 related airfoil sections from tests in the variable-density wind tunnel*, Report 460, National Advisory Committee for Aeronautics, **1933**.

[17] M. Haussmann, A. C. Barreto, G. L. Kouyi, N. Rivière, H. Nirschl, M. J. Krause, *Comput. Math. Appl.* **2019**, *78 (10)*, 3285–3302. DOI: https://doi.org/10.1016/j.camwa.2019.04.033

[18] D. R. Chapman, *AIAA J.* **1979**, *17 (12)*, 1293–1313. DOI: https://doi.org/10.2514/3.61311

[19] F. Löffler, *Staubabscheiden*, Lehrbuchreihe Chemieingenieurwesen / Verfahrenstechnik, Thieme, Stuttgart **1988**.